

Ultrafast photocurrents at the surface of the three-dimensional topological insulator Bi_2Se_3

Lukas Braun,¹ Gregor Mussler,² Andrzej Hruban,³ Marcin Konczykowski,⁴ Thomas Schumann,⁵ Martin Wolf,¹ Markus Münzenberg,⁵ Luca Perfetti,⁴ and Tobias Kampfrath¹

¹*Fritz Haber Institute of the Max Planck Society, 14195 Berlin, Germany*

²*PGI-9 and JARA-FIT, Forschungszentrum Jülich, 52425 Jülich, Germany*

³*Institute of Electronic Materials Technology, 01-919 Warsaw, Poland*

⁴*Laboratoire des Solides Irradiés, CNRS UMR 7642 & CEA-DSM-IRAMIS, Ecole Polytechnique, F91128 Palaiseau, France*

⁵*Institut für Physik, Ernst-Moritz-Arndt Universität Greifswald, 17489 Greifswald, Germany*

(Dated: April 11, 2018)

Topological insulators constitute a new and fascinating class of matter with insulating bulk yet metallic surfaces that host highly mobile charge carriers with spin-momentum locking. Remarkably, the direction and magnitude of surface currents can be controlled with tailored light beams, but the underlying mechanisms are not yet well understood. To directly resolve the “birth” of such photocurrents we need to boost the time resolution to the scale of elementary scattering events (~ 10 fs). Here, we excite and measure photocurrents in the three-dimensional model topological insulator Bi_2Se_3 with a time resolution as short as 20 fs by sampling the concomitantly emitted broadband THz electromagnetic field from 1 to 40 THz. Remarkably, the ultrafast surface current response is dominated by a charge transfer along the Se-Bi bonds. In contrast, photon-helicity-dependent photocurrents are found to have orders of magnitude smaller magnitude than expected from generation scenarios based on asymmetric depopulation of the Dirac cone. Our findings are also of direct relevance for optoelectronic devices based on topological-insulator surface currents.

Many efforts in current solid-state research aim at pushing the speed of electronic devices from the gigahertz to the terahertz (1 THz = 10^{12} Hz) range¹ and at extending their functionalities by the spin of the electron.² In these respects, three-dimensional topological insulators (TIs) are a highly promising material class. While having an insulating bulk, their surface is metallic due to a band inversion that is topologically protected against external perturbations. Bi_2Se_3 is a model TI³ as its surface features a single pair of linear Dirac-type electron energy bands⁴ with spin-velocity locking and forbidden 180° backscattering.⁵ These properties are ideal prerequisites to achieve large surface-current-induced spin polarizations.

Part of this large potential was demonstrated by recent works. They reported the exciting possibility of launching TI surface currents by simply illuminating the sample with light.^{6–13} The direction of the photocurrent could be controlled through the polarization of the incident light beam. The assignment to a surface process was bolstered by picosecond time-of-flight measurements¹³ showing that the ballistic photoinduced carriers were propagating at a speed comparable to the band velocity of the Dirac states. There is, however, still an intense debate about mechanisms leading to TI surface currents. Scenarios based on asymmetric depopulation of the Dirac cone,⁶ transitions into other, higher-lying cones¹³ and asymmetric scattering of electrons⁸ have been proposed. To directly resolve the generation of TI surface photocurrents, we need to boost the time resolution of the experiment from so far ~ 250 fs and longer^{9–13} to the scale of elementary scattering events, which can be shorter than 10 fs.

Here, we use ultrabroadband THz emission spec-

troscopy^{14–16} from 0.3 to 40 THz to probe the ultrafast evolution of photocurrents in the model TI Bi_2Se_3 with unprecedented time resolution. We identify distinct current sources: first, a slow drift of photoinduced bulk charge carriers in the TI surface field. Second, for the first time, we observe a new type of photocurrent, a surface shift current, which originates from an instantaneous displacement of electron density along the Se-Bi bond. This current represents a dominant charge-transfer excitation localized in a surface region of ~ 3 nm thickness, which is the natural confinement scale of topological edge states. The modified electron density redistributes with a time constant of 22 fs. Finally and remarkably, currents depending on the pump helicity are found to have orders of magnitude smaller magnitude than expected from generation scenarios based on asymmetric depopulation of the Dirac cone⁶ (Fig. 3d). This result is not in contradiction to the previous observation of such currents in time-integrating experiments.⁶ However, it shows that the generation of pump-helicity-dependent photocurrents is surprisingly slow, thereby pointing to noninstantaneous processes⁸ that are clearly distinct from the proposed instantaneous depopulation scenario.

RESULTS

Ultrafast photocurrent amperemeter. Our experimental setup is schematically depicted in Fig. 1a. A femtosecond laser pulse incident on the specimen launches a transient charge current density $\mathbf{j}(z, t)$. This photocurrent, in turn, emits an electromagnetic pulse with transient electric field $\mathbf{E}(t)$, in particular covering frequencies up to the THz range, as expected from the

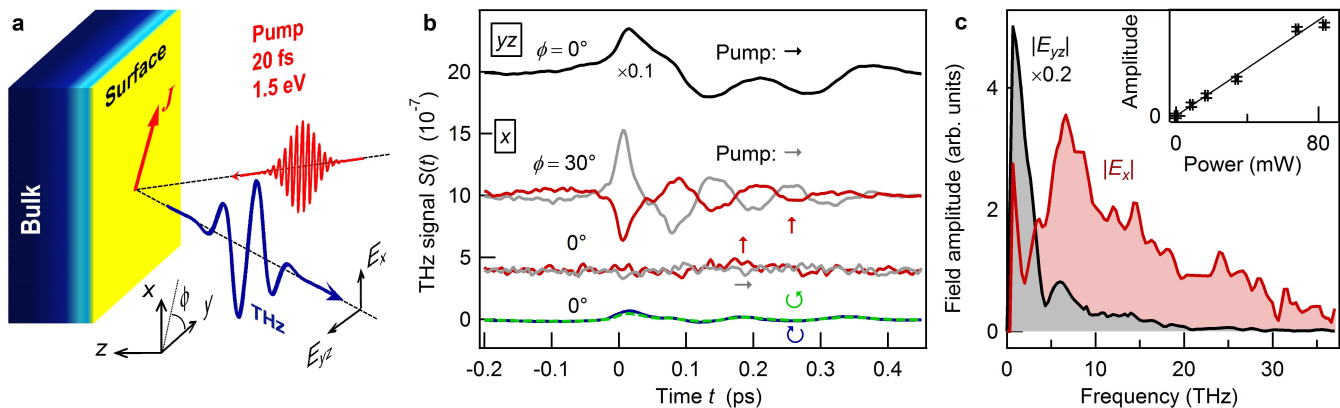


FIG. 1. Ultrafast photocurrent amperemeter: schematic and raw data. **a**, A Bi_2Se_3 crystal is excited by a femtosecond laser pulse, resulting in a photocurrent burst and, consequently, emission of a THz electromagnetic pulse. Measurement of the transient THz electric field components $E_x(t)$ and $E_{yz}(t)$ by electrooptic sampling provides access to the sheet current $\mathbf{J}(t)$ flowing inside the sample. **b**, Typical x - and yz -polarized THz signals for various settings of pump polarization and sample azimuth ϕ . Signals are offset for clarity. **c**, Amplitude spectra of the THz electric field directly behind the sample as extracted from time-domain signals of panel **b** (see text).

inverse duration of the femtosecond stimulus. The measurement of $\mathbf{E}(t)$ over a large bandwidth (0.3 to 40 THz) permits extraction of the sheet current density

$$\mathbf{J}(t) = \int dz \mathbf{j}(z, t) \quad (1)$$

with ultrafast time resolution. More precisely, this approach allows us to separately determine the current component J_x directed along the x -axis and the component J_{yz} , which is a linear combination of the Cartesian components J_y and J_z (Fig. 1a). By virtue of a generalized Ohm's law, the currents J_x and J_{yz} are, respectively, connected to the x -polarized electric-field component E_x and the perpendicular component E_{yz} directly behind the sample (Fig. 1a). The THz near-fields E_x and E_{yz} are, respectively, obtained by measuring the THz far-field using electrooptic sampling, resulting in the electrooptic signals S_x and S_{yz} , respectively (see Methods). THz waveforms are acquired for various settings of the pump polarization and sample azimuth ϕ (Fig. 1a).

We use this approach to study a freshly cleaved, n -type Bi_2Se_3 single crystal in ambient air (see Methods). While photocurrents in the inversion-symmetric crystal bulk (space group D_{3d}^5) cancel, optical excitation can in principle launch a current at the surface (space group C_{3v}).¹⁷ The surface region can be thought of as being comprised of the air-crystal interface with locally relaxed lattice structure and simultaneously hosting the Dirac surface states (thickness of ~ 2 nm),^{18,19} followed by a space-charge region with bent bulk bands (thickness of tens of nanometers).^{20,21}

In the following, we will show that our broadband current measurements allow us to discriminate different types of photocurrents and their generation in the various surface regions. This goal is achieved by first identifying two dominating components in the THz emission signal

using symmetry analysis. Based on the temporal structure of the two underlying photocurrent components, we can finally assign these to microscopic generation scenarios.

Raw data. Typical THz electrooptic signal waveforms $S(t)$ from our Bi_2Se_3 sample are shown in Fig. 1b. The THz waveforms depend sensitively on the setting of the THz polarization (x vs yz), the pump polarization and the sample azimuthal angle ϕ . The signal amplitude grows linearly with increasing pump power, without any indication of saturation (inset of Fig. 1c). This behavior implies that the number of excited carriers is proportional to the incident photon number.

As detailed in the following, we make the striking observation that the x - and yz -polarized components of the emitted THz field (and, thus, J_x and J_{yz}) behave very differently in terms of their magnitude (Fig. 1b), temporal shape (Fig. 1b), behavior after sample cleavage (Fig. 2a) and azimuth-dependence (Fig. 3a). First, as seen in Fig. 1b, S_{yz} exhibits much larger amplitude than S_x but evolves significantly more slowly. This trend becomes even clearer when we apply an inversion procedure to these data to extract the THz fields E_x and E_{yz} directly behind the sample (see Methods). The resulting spectral amplitudes are displayed in Fig. 1c as a function of angular frequency ω and show that $|E_x(\omega)|$ is much broader than $|E_{yz}(\omega)|$, indicating much faster temporal dynamics.

Second, to investigate the impact of surface modification on S_x and S_{yz} , we freshly cleave the sample and subsequently acquire THz signals continuously over 2 h with the sample exposed to air. While the shape of the THz waveforms does not undergo measurable modifications, its global amplitude increases by a factor of ≈ 2 in the course of time (Fig. 2a). Note this rise proceeds within 30 min for S_x but significantly slower (within 100 min)

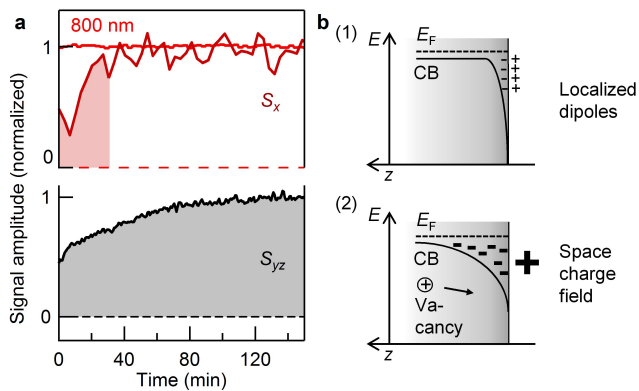


FIG. 2. Impact of sample cleaving on THz emission. **a**, Evolution of the amplitudes of THz signals S_x and S_{yz} and the reflectance of the 800 nm pump beam. The latter remains unchanged showing that no sample damage occurs. **b**, Schematic of two symmetry-breaking processes triggered by sample cleaving, (1) formation of localized surface electric dipoles and (2) band bending due to migration of charged bulk Se vacancies toward the surface.

for S_{yz} . We will later relate this observation to distinct surface modification processes and use this information to estimate the degree of surface localization of the currents J_x and J_{yz} . In contrast to S_x and S_{yz} , measurable changes of the sample reflectance at a wavelength of 800 nm are not observed, thereby ruling optical degradation of our sample out.

Signal symmetries. In addition to their different amplitude and temporal structure, S_x and S_{yz} also depend very differently on the sample azimuth ϕ (Fig. 1a). To quantify this behavior, we measure waveforms $S_x(t, \phi)$ and $S_{yz}(t, \phi)$ for an extended set of ϕ -values. To reliably extract an average signal amplitude for each ϕ , we project the time-domain signal on a suitable reference waveform (see Supplementary). The resulting signal amplitude as a function of ϕ is displayed in Fig. 3a. While S_x is almost fully modulated with a periodicity of $2\pi/3 = 120^\circ$, S_{yz} is dominated by a constant offset.

The threefold rotational symmetry of the THz signals is consistent with the symmetry groups of sample surface and bulk.³ Importantly, it allows us to significantly reduce the large amount of experimental data contained in $S(t, \phi)$: for a given THz polarization (x or yz) and pump polarization, each two-dimensional set $S(t, \phi)$ can be written as a linear combination of just three basis functions (see Supplementary),

$$S(t, \phi) = A(t) + B(t) \sin(3\phi) + C(t) \cos(3\phi). \quad (2)$$

Therefore, three basis signals $A(t)$, $B(t)$ and $C(t)$ fully characterize the entire data set $S(t, \phi)$. They are, respectively, obtained by projecting $S(t, \phi)$ onto the mutually orthogonal functions 1, $\sin(3\phi)$ and $\cos(3\phi)$. Extracted waves are shown in Fig. 3b for the two THz polarizations and various pump polarizations.

We begin with considering the impact of the pump

helicity on the photocurrent. The bottommost curve in Fig. 3b represents the ϕ -independent $A_x(t)$ of the difference of the signals taken with right-handed (\odot) and left-handed (\ominus) circularly polarized pump light. The amplitude of this waveform is comparable to the noise floor. In other words, a helicity-dependent yet simultaneously ϕ -independent THz signal is small and below our detection threshold. This notion is consistent with time-domain raw data (blue vs green trace in Fig. 1b) and the absence of an offset in the ϕ -dependence (blue curve of Fig. 3a). We note that such small magnitude of the pump-helicity-dependent and ϕ -independent photocurrent does not contradict the previously reported observation of time-integrated currents⁶ as will be discussed further below.

Photocurrents and assignment. Figure 3b leads to another important conclusion of our symmetry analysis: regardless of the pump polarization, all signals S_x and S_{yz} are, respectively, dominated by just one fast and one slow waveform. We use these signals to extract the underlying source currents (see Supplementary) which are displayed in Fig. 3c. After an initial onset, both J_x and J_{yz} change sign, indicating a backflow of charge. Note, however, J_x proceeds on a much faster time scale than J_{yz} : the rise time from 10% to 90% current maximum is 16 fs for J_x vs 120 fs for J_{yz} . The respective decay time constant are 27 fs vs 200 fs.

To determine the origin of J_x and J_{yz} based on their ultrafast dynamics, we briefly review known photocurrent generation mechanisms.^{6,8,22–29} In general, optical excitation transfers electrons from initial states $|i\rangle$ into final states $|f\rangle$ [Fig. 3(d)], followed by relaxation processes such as scattering into other states, phonon emission and recombination.³⁰ Photocurrents can arise in both regimes, that is, during the optical transition and during the subsequent relaxation. As our pump photon energy (1.57 eV) is much larger than the Bi_2Se_3 band gap, numerous vertical interband transitions are allowed³¹ and expected to outnumber the contribution of phonon- or impurity-assisted nonvertical transitions.³² To obtain a macroscopic net current, inversion symmetry needs to be broken. In the relaxation regime, currents can arise from, for instance, scattering by a noncentrosymmetric potential,^{8,23} asymmetric recombination³³ and carrier acceleration in an intrinsic surface field (drift current).^{34,35}

As seen in Fig. 3c, the slow current $J_{yz}(t)$ has a first peak (width of 120 fs) much wider than the excitation pulse. Therefore, J_{yz} cannot arise from the initial optical transition. In fact, previous works on Bi_2Se_3 assigned the J_{yz} component to a carrier drift in the surface field, consistent with the strong dependence of J_{yz} on the doping level of Bi_2Se_3 .^{9–11} The double-peak structure of J_{yz} indicates complex relaxation dynamics possibly involving strongly damped plasma oscillations.³⁵ These aspects are beyond the scope of this work, and we focus now on the very fast, sub-100 fs photocurrent dynamics of J_x .

Along these lines, Sipe *et al.*^{22,36} used perturbation theory to identify three distinct mechanisms of photocur-

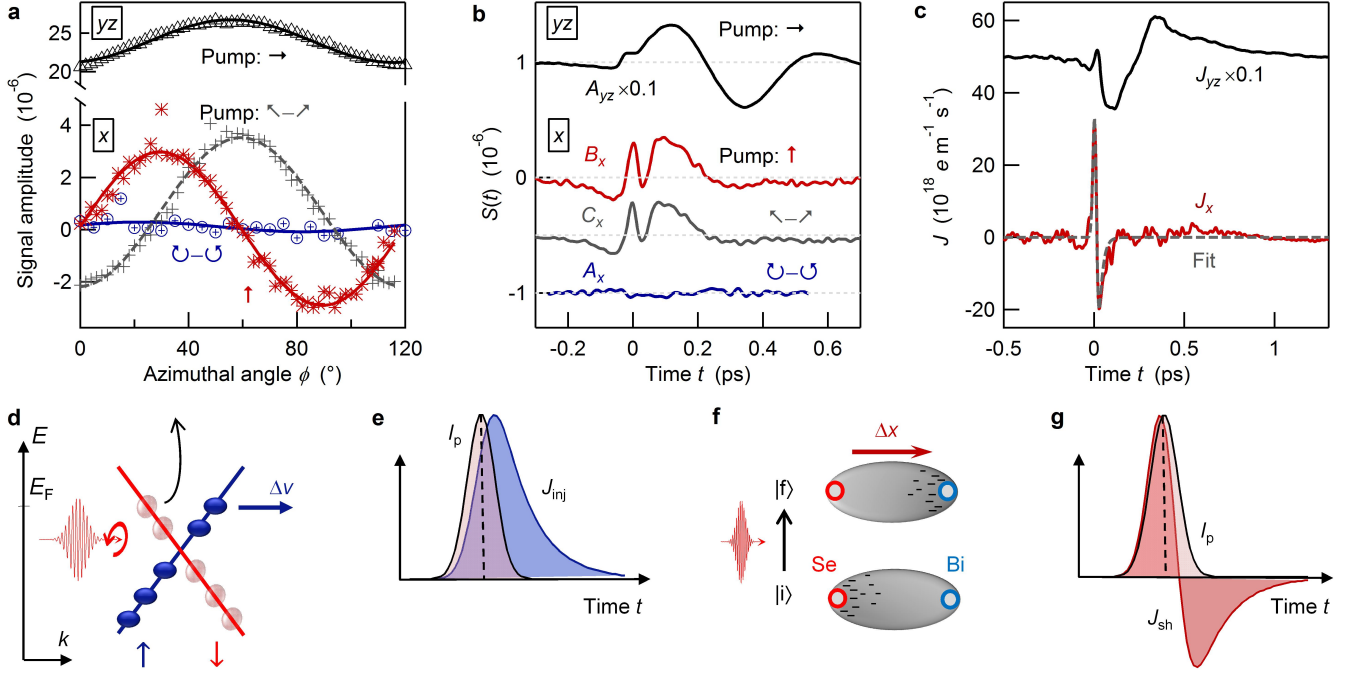


FIG. 3. Extraction of the dominant photocurrents and assignment. **a**, THz signal amplitude versus sample azimuth ϕ for various settings of the pump polarization (\rightarrow , \uparrow and differential signals $\nwarrow - \nearrow$ and $\circ - \odot$). While S_x exhibits a strong 3ϕ -type-dependence, S_{yz} is nearly independent of ϕ . **b**, Dominant temporal components of signal sets $S_{yz}(t, \phi)$ and $S_x(t, \phi)$ for various pump polarizations, extracted using Eq. (2). **c**, Source currents of the two dominant signal components. The dynamics of these currents allow us to reveal the origin of the photocurrent. **d**, Example of an injection-type photocurrent. The pump pulse promotes electrons from the Dirac cone into other bands, thereby changing the electron band velocity. An asymmetric depopulation of the Dirac cone and, thus, nonzero net current is achieved by using circularly polarized light. **e**, Expected unipolar time-dependence of an injection-type photocurrent $J_{\text{inj}}(t)$ driven by a laser pulse with intensity envelope $I_p(t)$. **f**, Scenario of a shift photocurrent arising from an ultrafast transfer of electron density along the Se-Bi bond. **g**, Resulting bipolar temporal shape of the sheet current density $J_{\text{sh}}(t)$. Signals in **b** and **c** are offset for clarity.

rent generation by an optical transition $|i\rangle \rightarrow |f\rangle$: injection currents, shift currents and optical rectification. *Injection currents* J_{inj} arise because initial and final state of the perturbed electron have different band velocity. An example is the asymmetric band depopulation scenario⁶ shown in Fig. 3d: a circularly polarized pump excites electrons from the Dirac cone into higher-lying states with different band slope (group velocity). Therefore, for short enough excitation, J_{inj} should rise instantaneously to a magnitude that scales with the average velocity change Δv and the density N of the excited electrons. In this simplified model, the resulting current is

$$J_{\text{inj}} = \sigma_{\text{inj}} \Delta v [\Theta(t) e^{-t/\tau_{\text{inj}}}] * I_p \quad (3)$$

where the initial sheet charge density $\sigma_{\text{inj}} = eN\Delta z_{\text{inj}}$ is proportional to the thickness Δz_{inj} of the emitting sheet. Furthermore, $\Theta(t)$ is the unit step function, and the exponential accounts for relaxation of the current with time constant τ_{inj} . Backflow of electrons is diffusive³⁷ and ignored on the short timescales considered here. Finally, the convolution with the pump intensity envelope $I_p(t)$ (normalized to unity) accounts for the shape of the pump

pulse.

*Shift currents*³⁸, on the other hand, arise when the electron density distribution of the excited state $|f\rangle$ is spatially shifted with respect to $|i\rangle$ (Fig. 3f). For short excitation, this process leads to a step-like charge displacement $\Delta x_{\text{sh}}\Theta(t)$ whose temporal derivative is proportional to the shift current J_{sh} . With arguments analogous to the injection case, we obtain

$$J_{\text{sh}} = \sigma_{\text{sh}} \Delta x \frac{\partial}{\partial t} [\Theta(t) e^{-t/\tau_{\text{sh}}}] * I_p, \quad (4)$$

with $\sigma_{\text{sh}} = eN\Delta z_{\text{sh}}$. This model implies J_{sh} initially follows the profile of $I_p(t)$ and becomes bipolar if the relaxation time τ_{sh} is comparable to or longer than the pump duration (Fig. 3g). Finally, *optical rectification* can be understood as a nonresonantly driven virtual charge displacement. This effect is typically two orders of magnitude smaller than resonant optical transitions³⁹ and will not be considered further.

Note the characteristic shape of the ultrafast currents J_{inj} and J_{sh} is very distinct: unipolar (Fig. 3e) and bipolar asymmetric (Fig. 3g). Having understood how the

temporal shape of a current is intrinsically linked to its origin, we now look for such fingerprints in our data (Fig. 3c). Indeed, we find that the measured photocurrent J_x (Fig. 3c) has bipolar asymmetric temporal shape, the unambiguous fingerprint of a shift current. In addition, fitting Eq. (4) to J_x yields excellent agreement (Fig. 3c) for a pump duration of 23 fs, $\tau_{\text{sh}} = 22$ fs and $\Delta x_{\text{sh}} \Delta z_{\text{sh}} \approx 36 \text{ \AA}^2$. In this procedure, we use the excitation density ($N = 6.9 \times 10^{24} \text{ m}^{-3}$) as inferred from the absorbed pump fluence ($4 \mu\text{J cm}^{-2}$), the pump photon energy (1.57 eV) and the pump penetration depth (24 nm at 1/e intensity).²⁰ The thickness Δz_{sh} of the shift-current sheet will be determined next.

Surface localization. Our photocurrent measurements directly reveal an ultrafast shift current and a drift current in the time domain. It is so far, however, unclear to which extent these currents are localized at the surface. Although second-order optical probes such as THz emission and sum-frequency generation are only operative at the surface⁴⁰ of samples with inversion-symmetric bulk, the region of broken inversion symmetry extends over a certain depth. For example, the bulk drift current dominating J_{yz} (Fig. 3c) is known to flow in a layer whose thickness is given by the Thomas-Fermi screening length of the surface depletion field, which is ~ 16 nm in our sample.²⁰

Proving surface sensitivity is a well-known issue of nonlinear optics and has a common solution^{10,40}: modify the sample surface and monitor the impact on the signal. We modify the Bi_2Se_3 surface by cleaving, which is known to trigger transport processes on a time scale of 100 min.^{6,10} Extensive studies on such Bi_2Se_3 aging effects^{20,21,41,42} revealed two mechanisms (see schematic of Fig. 2b): (1) formation of an electric-dipole layer due to charge transfer from adsorbates^{21,42} or surface lattice relaxation¹⁹ and (2) migration of bulk defects, mainly Se vacancies, toward the surface.^{21,41} While the surface dipole layer is very localized (thickness of ~ 3 nm),²¹ the redistribution of bulk Se vacancies induces a more extended space-charge region (thickness of tens of nanometers).^{21,41}

We now relate these processes to the amplitude evolution of J_{yz} and J_x following sample cleaving (Fig. 2a). The drift current amplitude J_{yz} , intrinsically linked to the strength of the space-charge field, follows the redistribution of Se vacancies within 100 min. In contrast, J_x rises much faster (30 min), thereby showing that J_x originates from a layer in which a competing process dominates the signal modification. Consequently, we assign the fast time scale of J_x to the formation of the localized surface dipoles, suggesting J_x flows in a surface layer with a thickness Δz_{sh} of less than 3 nm. This value and the above extracted estimate for $\Delta x_{\text{sh}} \Delta z_{\text{sh}}$ imply the shift distance Δx_{sh} is on the order of 1 Å.

DISCUSSION

Summarizing our results, we have shown that our ultrabroadband THz emission data are fully consistent with the notion that (i) the photocurrent J_x arises from an instantaneous photoinduced shift of charge density by $\sim 1 \text{ \AA}$ in a ~ 3 nm thick surface region of Bi_2Se_3 . The displacement relaxes on a very fast time scale of 22 fs. The much slower current J_{yz} is dominated by a drift current of optically excited carriers in the surface field. (ii) A helicity-dependent and simultaneously azimuth-independent photocurrent is smaller than our detection threshold of $10^{18} \text{ e m}^{-1} \text{ s}^{-1}$. This assertion is also valid for other injection-type transport scenarios such as photon-drag currents.²⁵ It is instructive to discuss these observations and compare them to previous works.

Surface shift currents. Finding (i) represents the first observation of a surface shift current, which was theoretically predicted by Cabellos *et al.* very recently.⁴³ We emphasize that revealing the time-domain fingerprint of shift currents relies on the 20 fs time resolution of our experiment. Longer pump pulses can easily obscure this signature, even in materials with broken bulk inversion symmetry.⁴⁴ The threefold azimuthal symmetry of J_x (Fig. 3a) suggests the electron density is displaced along the 120°-ordered p-type Se-Bi bonds.⁴⁵ As Bi and Se atoms lie in different layers, the shift current also has a z -component with a strength comparable to J_x , consistent with the sharp peak present in J_{yz} at -10 fs [Fig. 3(c)].

Our results show that the displacement of bound charges occurs in a sheet with thickness $\Delta z_{\text{sh}} \sim 3$ nm. This notion is consistent with reports¹⁹ showing that only the first quintuple layer exhibits inversion asymmetry on the order of 10%. This fact indicates that the current is generated in a layer where the Dirac states are expected to dominate transport.¹⁸ The shift distance $\Delta x_{\text{sh}} \sim 1 \text{ \AA}$ compares well to reported charge shifts on the order of the bond length ($\sim 3 \text{ \AA}$) in noncentrosymmetric semiconductors.³⁸ In addition, the electron density associated with the Dirac states is known to shift from Se toward Bi atoms when energies below and above the Dirac point are considered.^{3,45} The charge shift relaxes within 22 fs which coincides with the time scale known for depopulation of the optically populated antibonding states.³⁰ Therefore, the assignment of J_x to a surface shift current is fully compatible with previous works.

Helicity-dependent currents. Result (ii), the absence of a circular photocurrent, is surprising and imposes significant constraints on the generation mechanism and shape of this current. McIver *et al.* observed a helicity-dependent time-integrated photocurrent and suggested it to arise from asymmetric depopulation of the Dirac cone by optical transitions into rapidly decaying bulk states (Fig. 3f). Based on this injection-type scenario, we use Eq. (3) to estimate the initial ballistic sheet-

current density as $Nev_D\Delta z_D$, where $v_D = 0.5 \text{ nm fs}^{-1}$ is the band velocity in the Dirac cone,³⁰ $\Delta z_D = 2 \text{ nm}$ the “thickness” of the Dirac states,¹⁸ and N is the excitation density. The resulting magnitude of $10^{22} \text{ e m}^{-1} \text{ s}^{-1}$ is four orders of magnitude larger than the maximum current measured in our experiment. Therefore, our measurements render the simple asymmetric-depopulation scenario very unlikely.

This result is supported by comparing the magnitudes of the helicity-dependent photocurrent seen in the time-integrated⁶ and in our time-resolved measurements. Assuming the transient current has rectangular temporal shape with amplitude J_0 and duration τ_0 , a time-integrated measurement⁶ yields an average sheet-current density of $\bar{J} = J_0\tau_0 f_{\text{rep}}$, where $f_{\text{rep}} \sim 100 \text{ MHz}$ is the repetition rate of commonly used femtosecond laser oscillators. For small \bar{J} and long τ_0 , J_0 may drop below our detection threshold of $10^{18} \text{ e m}^{-1} \text{ s}^{-1}$. Using the value $\bar{J} \sim 10^{13} \text{ e m}^{-1} \text{ s}^{-1}$ obtained in Ref. 6 under excitation conditions similar to ours, we find the helicity-dependent current must flow for a duration $\tau_0 > 100 \text{ fs}$ to be below our detection threshold. Such a relatively long current lifetime is not in favor of the asymmetric depopulation scenario (Fig. 3f)⁶ since the asymmetry of photo-generated holes in the Dirac cone is known to decay on a 40 fs time scale.⁴⁶ Therefore, our observations point to indirect and slower generation mechanisms of pump-helicity-dependent photocurrents, for example asymmetric electron scattering, as proposed for near-equilibrium electrons.⁸

In conclusion, we have measured the dynamics of ultrafast photocurrents on the surface of the three-dimensional model TI Bi_2Se_3 with a time resolution as short as 20 fs. We find that the peak amplitude of pump-helicity-dependent photocurrents is much smaller than predicted based on previous models. Its duration is inferred to exceed 100 fs. These results point to noninstantaneous generation mechanisms of the pump-helicity-dependent photocurrent and call for improved models and theories. In addition, we have for the first time observed a surface shift photocurrent which arises from a charge displacement on the TI surface. This current is potentially interesting for ultrafast optical manipulation of the TI surface, ultimately thereby modifying its topological properties.⁴⁷ Finally, our results highlight broadband THz emission spectroscopy as a novel and highly sensitive probe of surfaces.

METHODS

Sample details. Single crystals of Ca-doped Bi_2Se_3 were grown by the Bridgman-Stockbarger method by pulling a sealed quartz ampoule in a vertical tem-

perature gradient. Hall measurements⁴⁸ yield a bulk hole density of $1.34 \times 10^{17} \text{ cm}^{-3}$ and a mobility of $275 \text{ cm}^2 \text{ V}^{-1} \text{ s}^{-1}$. From angle-resolved photoelectron spectroscopy (ARPES), we extract a conduction-band electron mass of 0.115 bare electron masses.⁴⁹ A fresh surface is obtained by cleaving using adhesive tape. After exposition to air, ARPES measurements confirm the presence of Dirac surface states with the Fermi energy located 160 meV above the bulk conduction band minimum.

Ultrafast amperemeter. Laser pulses (duration of $\approx 20 \text{ fs}$, center wavelength of 800 nm, energy 1 nJ) from a Ti:sapphire oscillator (repetition rate 80 MHz) are focused onto the sample (beam diameter of 200 μm full-width at half intensity maximum) under 45° angle of incidence, resulting in an average intensity $< 0.3 \text{ kW cm}^{-2}$, well below sample damage threshold. The specularly emitted THz pulse is focused onto an electrooptic crystal in which the THz electric field is detected by broadband electrooptic sampling.⁵⁰ We use a (110)-oriented GaP crystal (thickness of 250 μm) owing to its relatively flat and broadband response function.¹⁶ The only exception are the measurements of the two-dimensional data set $S(t, \phi)$ (Figs. 3a and 3b) which are sped up by using (110)-oriented ZnTe crystal (thickness of 300 μm) having an enhanced detector response at the expense of reduced bandwidth.

To proceed from the measured electrooptic signal $S(t)$ to the THz electric field $\mathbf{E}(t)$ directly behind the sample, we also measure the transfer function of our spectrometer (see Supplementary). We finally obtain the source current $\mathbf{J}(t)$ by employing a generalized Ohm’s law (see Supplementary). Optical wave plates are used to set the polarization state of the pump pulse to circular or linear with arbitrary rotation angle. A THz wire-grid polarizer (field extinction ratio of 10^{-2}) allows us to measure the x - and yz -components E_x and E_{yz} of the THz electric field separately, thereby disentangling current components J_x and J_{yz} , the latter being a linear combination of J_y and J_z (Fig. 1a). To ensure the electrooptic THz detector has an identical response to E_x and E_{yz} , a wire-grid polarizer with 45° orientation is placed in front of it.

ACKNOWLEDGMENTS

We thank S.D. Ganichev, A.D. Bristow and N.P. Armitage for stimulating and fruitful discussions. We are grateful to the German Science Foundation (DFG) for financial support through priority program SPP 1666 “Topological insulators: materials, fundamental properties, devices” (grant no. KA 3305/3-1). L.P. and M.K. thank for support by grant ANR-13-IS04-0001-01.

¹ del Alamo, J. A. Nanometre-scale electronics with III-V compound semiconductors. *Nature* **479**, 317–323 (2011).

² Stamps, R. L. *et al.* The 2014 magnetism roadmap. *J. Phys. D: Appl. Phys.* **47**, 333001 (2014).

- ³ Zhang, H. *et al.* Topological insulators in Bi₂Se₃, Bi₂Te₃ and Sb₂Te₃ with a single Dirac cone on the surface. *Nat. Phys.* **5**, 438–442 (2009).
- ⁴ Qi, X.-L. & Zhang, S.-C. Topological insulators and superconductors. *Rev. Mod. Phys.* **83**, 1057–1110 (2011).
- ⁵ Moore, J. E. The birth of topological insulators. *Nature* **464**, 194–198 (2010).
- ⁶ McIver, J. W., Hsieh, D., Steinberg, H., Jarillo-Herrero, P. & Gedik, N. Control over topological insulator photocurrents with light polarization. *Nat. Nanotechnol.* **7**, 96–100 (2012).
- ⁷ Duan, J. *et al.* Identification of helicity-dependent photocurrents from topological surface states in Bi₂Se₃ gated by ionic liquid. *Sci. Rep.* **4** (2014).
- ⁸ Olbrich, P. *et al.* Room-temperature high-frequency transport of Dirac fermions in epitaxially grown Sb₂Te₃- and Bi₂Te₃-based topological insulators. *Phys. Rev. Lett.* **113**, 096601 (2014).
- ⁹ Luo, C. W. *et al.* THz generation and detection on Dirac fermions in topological insulators. *Adv. Opt. Mater.* **1**, 804–808 (2013).
- ¹⁰ Zhu, L.-G., Kubera, B., Fai Mak, K. & Shan, J. Effect of surface states on terahertz emission from the Bi₂Se₃ surface. *Sci. Rep.* **5** (2015).
- ¹¹ Tu, C.-M. *et al.* Manifestation of a second Dirac surface state and bulk bands in THz radiation from topological insulators. *Sci. Rep.* **5**, 14128 (2015).
- ¹² Bas, D. A. *et al.* Coherent control of injection currents in high-quality films of Bi₂Se₃. *Appl. Phys. Lett.* **106**, 041109 (2015).
- ¹³ Kastl, C., Kärnetzky, C., Karl, H. & Holleitner, A. W. Ultrafast helicity control of surface currents in topological insulators with near-unity fidelity. *Nat. Commun.* **6** (2015).
- ¹⁴ Leitenstorfer, A., Hunsche, S., Shah, J., Nuss, M. & Knox, W. Detectors and sources for ultrabroadband electro-optical sampling: Experiment and theory. *Appl. Phys. Lett.* **74**, 1516–1518 (1999).
- ¹⁵ Leitenstorfer, A., Hunsche, S., Shah, J., Nuss, M. C. & Knox, W. H. Femtosecond charge transport in polar semiconductors. *Phys. Rev. Lett.* **82**, 5140–5143 (1999).
- ¹⁶ Kampfrath, T. *et al.* Terahertz spin current pulses controlled by magnetic heterostructures. *Nat. Nanotechnol.* **8**, 256–260 (2013).
- ¹⁷ Liu, C.-X. *et al.* Model Hamiltonian for topological insulators. *Phys. Rev. B* **82**, 045122 (2010).
- ¹⁸ Zhang, W., Yu, R., Zhang, H.-J., Dai, X. & Fang, Z. First-principles studies of the three-dimensional strong topological insulators Bi₂Te₃, Bi₂Se₃ and Sb₂Te₃. *New J. Phys.* **12**, 065013 (2010).
- ¹⁹ Roy, S. *et al.* Atomic relaxations at the (0001) surface of Bi₂Se₃ single crystals and ultrathin films. *Phys. Rev. B* **90**, 155456 (2014).
- ²⁰ McIver, J. W. *et al.* Theoretical and experimental study of second harmonic generation from the surface of the topological insulator Bi₂Se₃. *Phys. Rev. B* **86**, 035327 (2012).
- ²¹ Park, K., Beule, C. D. & Partoens, B. The ageing effect in topological insulators: evolution of the surface electronic structure of Bi₂Se₃ upon K adsorption. *New J. Phys.* **15**, 113031 (2013).
- ²² Nastos, F. & Sipe, J. E. Optical rectification and current injection in unbiased semiconductors. *Phys. Rev. B* **82**, 235204 (2010).
- ²³ Belinicher, V. I. & Sturman, B. I. The photogalvanic effect in media lacking a center of symmetry. *Sov. Phys. Usp.* **23**, 199 (1980).
- ²⁴ Lewis, R. A. A review of terahertz sources. *J. Phys. D: Appl. Phys.* **47**, 374001 (2014).
- ²⁵ Glazov, M. & Ganichev, S. High frequency electric field induced nonlinear effects in graphene. *Phys. Rep.* **535**, 101–138 (2014).
- ²⁶ Ganichev, S. D. *et al.* Resonant inversion of the circular photogalvanic effect in *n*-doped quantum wells. *Phys. Rev. B* **68**, 035319 (2003).
- ²⁷ Ivchenko, E. & Ganichev, S. Spin physics in semiconductors (2008).
- ²⁸ Schmidt, C. B., Priyadarshi, S., Tarasenko, S. A. & Bieler, M. Ultrafast magneto-photocurrents in GaAs: Separation of surface and bulk contributions. *Applied Physics Letters* **106**, – (2015).
- ²⁹ Priyadarshi, S., Pierz, K. & Bieler, M. All-optically induced ultrafast photocurrents: Beyond the instantaneous coherent response. *Phys. Rev. Lett.* **109**, 216601 (2012).
- ³⁰ Sobota, J. A. *et al.* Direct optical coupling to an unoccupied Dirac surface state in the topological insulator Bi₂Se₃. *Phys. Rev. Lett.* **111**, 136802 (2013).
- ³¹ Boschini, F. *et al.* Coherent ultrafast spin-dynamics probed in three dimensional topological insulators. *Sci. Rep.* **5**, 15304 (2015).
- ³² Weber, W. *et al.* Quantum ratchet effects induced by terahertz radiation in GaN-based two-dimensional structures. *Phys. Rev. B* **77**, 245304 (2008).
- ³³ Glass, A. M., von der Linde, D. & Negran, T. J. High-voltage bulk photovoltaic effect and the photorefractive process in LiNbO₃. *Appl. Phys. Lett.* **25**, 233–235 (1974).
- ³⁴ Johnston, M. B., Whittaker, D. M., Corchia, A., Davies, A. G. & Linfield, E. H. Simulation of terahertz generation at semiconductor surfaces. *Phys. Rev. B* **65**, 165301 (2002).
- ³⁵ Malevich, V. L., Adomavičius, R. & Krotkus, A. THz emission from semiconductor surfaces. *C. R. Phys.* **9**, 130–141 (2008).
- ³⁶ Sipe, J. E. & Shkrebti, A. I. Second-order optical response in semiconductors. *Phys. Rev. B* **61**, 5337–5352 (2000).
- ³⁷ Apostolopoulos, V. & Barnes, M. THz emitters based on the photo-Dember effect. *J. Phys. D: Appl. Phys.* **47**, 374002 (2014).
- ³⁸ Nastos, F. & Sipe, J. E. Optical rectification and shift currents in GaAs and GaP response: Below and above the band gap. *Phys. Rev. B* **74**, 035201 (2006).
- ³⁹ Côté, D., Laman, N. & Van Driel, H. Rectification and shift currents in GaAs. *Appl. Phys. Lett.* **80**, 905–907 (2002).
- ⁴⁰ Shen, Y.-R. *Principles of nonlinear optics* (Wiley-Interscience, New York, NY, USA, 1984).
- ⁴¹ Xu, C. *et al.* Intrinsic and extrinsic effects on the electrostatic field at the surface of Bi₂Se₃. *J. Appl. Phys.* **116**, 043519 (2014).
- ⁴² Benia, H. M., Lin, C., Kern, K. & Ast, C. R. Reactive chemical doping of the Bi₂Se₃ topological insulator. *Phys. Rev. Lett.* **107**, 177602 (2011).
- ⁴³ Cabellos, J. L., Mendoza, B. S. & Shkrebti, A. I. Optical coherent current control at surfaces: Theory of injection current. *Phys. Rev. B* **84**, 195326 (2011).
- ⁴⁴ Laman, N., Bieler, M. & Van Driel, H. Ultrafast shift and injection currents observed in wurtzite semiconductors via emitted terahertz radiation. *J. Appl. Phys.* **98**, 103507–103507 (2005).

- ⁴⁵ Mishra, S. K., Satpathy, S. & Jepsen, O. Electronic structure and thermoelectric properties of bismuth telluride and bismuth selenide. *J. Phys.: Condens. Matter* **9**, 461 (1997).
- ⁴⁶ Park, S. R. *et al.* Quasiparticle scattering and the protected nature of the topological states in a parent topological insulator Bi₂Se₃. *Phys. Rev. B* **81**, 041405 (2010).
- ⁴⁷ Liu, Q., Zhang, X., Abdalla, L., Fazzio, A. & Zunger, A. Switching a normal insulator into a topological insulator via electric field with application to phosphorene. *Nano Lett.* **15**, 1222–1228 (2015).
- ⁴⁸ Hruban, A. *et al.* Influence of chemical composition of liquid phase and growth process on physical properties of Bi₂Se₃, Bi₂Te₃ and Bi₂Te₂Se compounds. *Acta. Phys. Pol. A* **120**, 950–953 (2011).
- ⁴⁹ Xia, Y. *et al.* Observation of a large-gap topological-insulator class with a single Dirac cone on the surface. *Nat. Phys.* **5**, 398–402 (2009).
- ⁵⁰ Ferguson, B. & Zhang, X.-C. Materials for terahertz science and technology. *Nat. Mater.* **1**, 26–33 (2002).